Journal of Materials Chemistry A

Accepted Manuscript

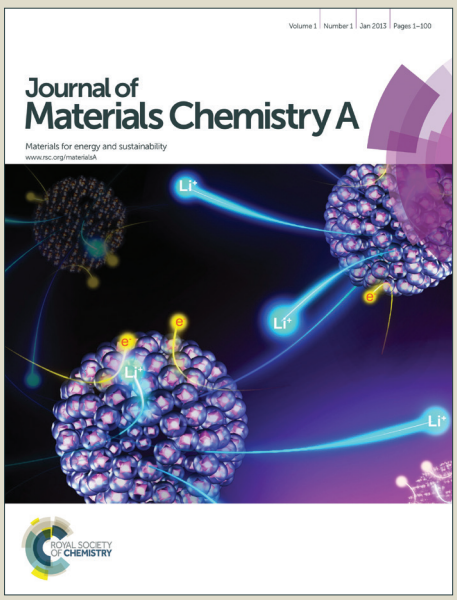

ROYAL SOCIETY OF CHEMISTRY

www.rsc.org/materialsA

Journal Name

ARTICLE

Revealing the Elemental-Specific Growth Dynamics of Pt-Cu Multipods by Scanning Transmission Electron Microscopy and Chemical Mapping

Received 00th January 20xx,
Accepted 00th January 20xx

DOI: 10.1039/x0xx00000x

www.rsc.org/

Yingying Jiang,[a,‡] Ting Bian,[a,‡] Fang Lin,[b,a] Hui Zhang,[a,*] Chuanhong Jin,[a,*] Z. Y. Li,[a,c] Deren Yang,[a] Ze Zhang[a]

In this work, we reported our experimental approach to reveal the detailed growth behavior of platinum (Pt)-copper (Cu) bimetallic multipod nanostructures in one-pot synthesis by analyzing the intermediate products from different stages by using aberration-corrected scanning transmission electron microscopy and the associated energy-dispersive X-ray spectroscopy. An element-specific growth trajectories of PtCu multipod nanostructure with compositional variation couples to geometric morphologies was observed: Pt_x-Cu_{1-x} multipods start from Pt-rich seeds ($x > 0.6$), evolve into Pt-Cu alloy phase ($x \approx 0.5$), and then form Pt-rich branches (with $x > 0.8$). This could be further explained on considering the different redox potentials of two metals and their interactions through underpotential deposition, galvanic replacement, and phase segregation. The observed combination of geometric morphologies and compositional variations may provide newstragies to potentially aid rational synthesis of alloy catalysts.

1. Introduction

Bimetallic nanocrystals, consisting of two metal elements, usually exhibit combinational properties between them due to the competitive or synergistic effects. They are regarded as promising building blocks towards the functional-orientated designs of materials.[1-10] Among them, Pt-based nanocrystals are one of the most widely investigated catalysts due to their potential applications in oil refinement, fine chemistry, fuel cell, etc.[11-13] In recent years, the combination of Pt with a "cheaper" metal M (M = Fe, Co, Ni, Cu, Mn, Ru, Pd, Au) has been adopted as a novel designing strategy for bimetallic nanocrystals for their enhanced catalytic activities and economical sensible choices.[14-30] Among them, Pt-Cu nanocrystals have been identified as a promising combination used as the catalyst for a variety of reactions such as methanol oxidation and oxygen reduction reaction. The last decade has witnessed the successful synthesis of Pt-Cu nanocrystals with a large number of shapes that dictated by the interactional effects between them such as underpotential deposition (UPD) and galvanic replacement. For example, Xie et al. demonstrated the synthesis of composition-tunable Pt-Cu octahedral nanocrystals through UPD.[31] Lou et al. reported the synthesis of $PtCu_3$ nanocages with enhanced electrocatalytic activity for methanol oxidation through galvanic replacement.[24] Pt-Cu concave nanocubes with high index facets and superior electrocatalytic activity were also synthesized through galvanic replacement by Yin et al.[32] In addition, Pt-Cu nanocubes, hollow nanocrystals, nanoframes, nanosheets, nanocones, multipods and so on were managed to be synthesized by solution-based approaches with high catalytic activities.[24, 33-39]

In spite of the significant progress which has been made on the precisely-controlled synthesis of Pt-Cu bimetallic nanocrystals with different structures, compositions, sizes and morphologies through the well-established solution-phase reduction of metal precursors, the detailed growth trajectories, like the elemental distributions, dynamics growth behaviors and corresponding growth mechanisms in different stages during growth, have been largely overlooked and thus poorly understood. For a system involving Pt and Cu, galvanic replacement and UPD may happen during nanocrystal growth due to the difference in electronegativity between Pt and Cu which will energetically favour the interaction of Pt-Cu bonds than Cu-Cu bonds. Both reactions have been used in controllable synthesis of Pt-Cu nanostructures as powerful strategies.[31-34] However, such reactions may accompany with the growth of Pt-Cu nanostructures, which makes it more complicated to clarify the growth paths and mechanisms of Pt-Cu systems.

[a] State Key Laboratory of Silicon Materials, School of Materials Science & Engineering and Cyrus Tang Center for Sensor Materials and Applications, Zhejiang University, Hangzhou, Zhejiang 310027, P. R. China
[b] College of Electronic Engineering, South China Agricultural University, Guangzhou, Guangdong 510642, P. R. China.
[c] Nanoscale Physics Research Laboratory, School of Physics and Astronomy, University of Birmingham, Birmingham B15 2TT, United Kingdom.
‡ These authors contribute equally to this work.
Electronic Supplementary Information (ESI) available: Additional characterization of Pt-Cu nanostructures, ICP-MS results and errors of EDS quantifications. See DOI: 10.1039/x0xx00000x

To address these issues, we carried out systematically a microscopic study on the growth of Pt-Cu nanocrystals by means of high angle annular dark field (HAADF) scanning transmission electron microscopy (STEM) imaging and the associated energy-dispersive X-ray spectroscopy (EDS). The products during different stages of the solution-phase growth were collected and characterized by HAADF-STEM imaging and EDS mapping. By tracking both the structural evolution and compositional variation, we reveal a novel element-specific growth mechanism of Pt-Cu multipods where different alloying components follow different growth pathways, which is in contrary to the popular recognition of essentially homogeneous or monotonically variation of elemental distribution.

2. Experimental Section

Synthesis of Pt-Cu Multipods.

In a standard synthesis, 5 mL of OAm containing 30 mg CTAB and 100 mg TOPO was added to a glass vial, and pre-heated to 180 ^{o}C in air under magnetic stirring for 10 min. After that, 21.2 mg $Pt(acac)_2$ and 1.6 mg $Cu(acac)_2$ with a molar ratio of 9 : 1 were dissolved in 3 mL OAm. Subsequently, this precursor solution was injected into the pre-heated vial. The reaction was maintained at 180 ^{o}C for a certain amount of time. For comparison, we also performed another two groups of experiments by varying the molar ratio of Pt to Cu salt precursors. The first one is by varying the molar ratio of Pt to Cu salt precursors to 30 : 1 (22.8 mg $Pt(acac)_2$ and 0.5 mg $Cu(acac)_2$), the second one is in the absence of $Cu(acac)_2$ (23.6 mg $Pt(acac)_2$), with all other parameters being kept the same as those used in the standard procedure. We mark the standard synthesis with molar ratio of Pt to Cu precursors being 9 : 1 as group I (9 : 1), the first contrast experiment with molar ratio of Pt to Cu precursors being 30 : 1 as group II (30 : 1), the second contrast experiment in the absence of Cu precursor as group III for simplification.

Microscopy and Spectroscopy.

HAADF-STEM images and EDS analyses were conducted with a FEI-Titan ChemiSTEM operated at an acceleration voltage of 200 kV and equipped with a spherical aberration (C_s) corrector for probe side. A Bruker Super-X detector for X-ray was installed into this microscope, which could significantly increase the detection efficiency for chemical analysis. The typical recording time for each EDS map was set to 4 minutes. The illumination angle was 17.9 mrad with a probe current of 0.17 nA, and the collection angle ranges from 53 mrad to 200 mrad. All the measurements of projected areas were done with ImageJ (Fig. S1).

ICP-MS. The percentages of Pt and Cu in the samples were determined using inductively coupled plasma mass spectrometry (ICP-MS, Perkin-Elmer Elan DRC II ICP-MS).

3. Results and Discussion

Pt-Cu multipods were synthesized by co-reduction of Pt and Cu salt precursors in oleylamine (OAm) in the presence of cetyltrimethylammonium bromide (CTAB). Three groups of metallic multipods were synthesized with varying molar ratios of Pt and Cu precursors of 9 : 1 (group I), 30 : 1 (group II) and without Cu precursor (group III).

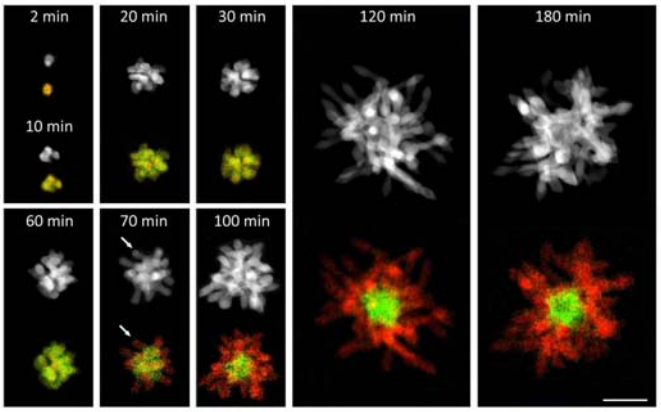

Fig. 1 Morphology and composition evolution of the growth trajectories of Pt-Cu multipods from group I (9 : 1). The growth process lasts for 180 minutes. The upper mono-chromatic images correspond to HAADF-STEM analysis, the lower colored images are the corresponding EDS mappings of Pt (red) and Cu (green) elements. The scale bars in all the panels are 30 nm.

A series of Pt-Cu samples obtained at different reaction times were collected for HAADF-STEM and EDS analysis. Fig. 1 shows the growth trajectories of Pt-Cu multipods in 180 minutes in group I (9 : 1). Low-magnification HAADF-STEM images are presented in Fig. S2. From the HAADF-STEM images, we can see the evolution of the Pt-Cu nanostructures from a simple polyhedron to flower-like shape, and then to complex structures with rod-like branches protruding from the core. During the initial growth period of 2 min, nearly spherical single crystals with composition of $Pt_{64}Cu_{36}$ are generated. The atomic composition of Pt and Cu has been measured from EDS quantification over a large number of particles at large areas. It should be noted that the results from EDS analysis were consistent with those from ICP-MS as shown in Tables S1 and S2. In the following 8 min, the small single crystals evolve into the nanostructures with several petals through growth. With the growth continues from 10 to 60 min, these nanocystals grow into more complex structures with more petals coming out. After 70 min, a dramatic change shows up, numerous branches with higher aspect ratio than petals which are composed of Pt-rich phase start to growth on the Pt-Cu alloy multipods indicated with arrows in Fig. 1 (HAADF-STEM and EDS mapping images of Pt-Cu nanostructures at higher magnification obtained at 60 and 70 min are shown in Fig. S3). From 70 to 180 min, the branches grow longer. From the EDS mapping images, we can deduce that the nanostructures are composed of Pt-Cu alloys in the first 60 min. After 60 min, the growing branches are composed of Pt-rich constituent, such as pointed area in 70 min of Fig. 1. At this time, galvanic replacement of Pt^{2+} ions with Cu atoms in the Pt-Cu alloy may happen due to its higher standard redox potential comparing with Cu^{2+} ions. Galvanic replacement may be one of the main

reasons causing morphology transition during growth process.[34] When the molar ratio of Pt to Cu precursor changes from 9 : 1 (group I) to 30 : 1 (group II), the morphology evolution and the elemental distribution (presented in Fig. S4 and S5) are similar except for the variation of the size compared to group I.

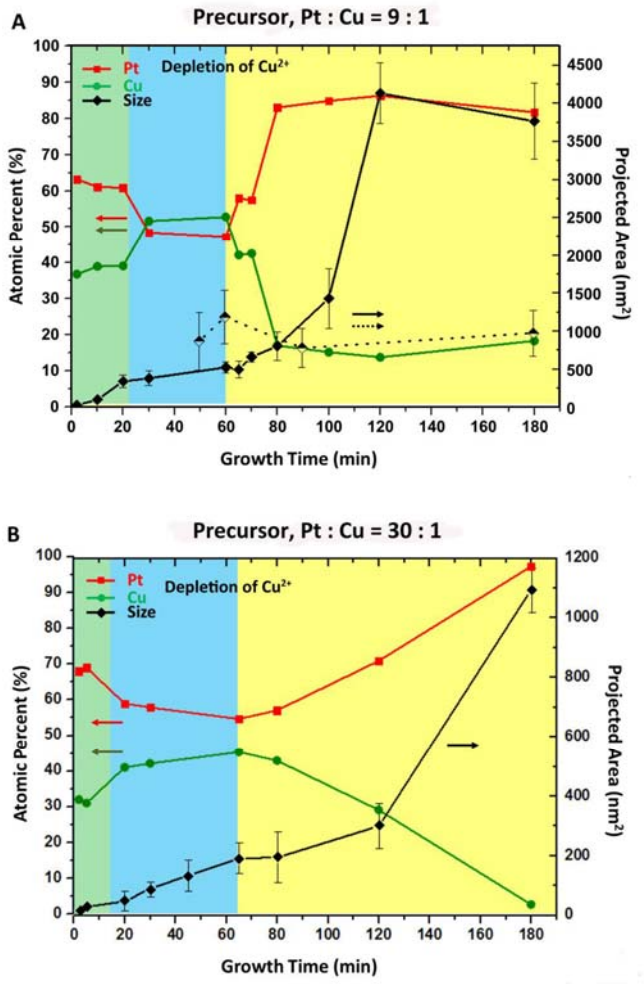

Fig. 2 Size and atomic percent evolutions of Pt-Cu multipods in group I (A) with precursors of Pt and Cu as 9 : 1 and group II (B) with precursors as 30 : 1. The red dots and corresponding connected lines represent the mean atomic percent of Pt element from EDS quantification results of hundreds of multipods after different growth periods, the green ones represent the mean atomic percent of Cu element. The black dots and corresponding connected lines in A are average size evolutions of Pt-Cu multipods during growth, and the half-hollow dots and the dotted lines are the size evolutions of Pt multipods without addition of Cu precursor (group III). The error bars for sizes are mean square errors calculated from the measured values of individual nanostructures in each group. Errors of EDS quantifications are listed in Table S2.

In order to gain more comprehensive information of Pt-Cu multipods during growth cycle, quantitative analysis of the size and elemental atomic ratio of Pt-Cu nanostructures in all groups at different reaction times are carried out as shown in Fig. 2. In group I (Fig. 2A), the atomic percent of Pt starts from 63% at 2 min, then drops slightly to ~60% and remains almost unchanged until 20 min, which is dramatically lower than the feeding ratio, 9 : 1. After 20 min reaction, the atomic percent of Pt drops to ~50% and keeps almost unchanged for further 30 minutes. At around 60 min, Pt content starts to arise rapidly to ~85% and maintains at this high level till the end of the reaction (180 min). The elemental Cu experiences a complementary variation in the atomic percent, in comparison with Pt. In addition, we monitored the reaction time-dependent size variation of Pt-Cu multipods during the growth. The size of Pt-Cu multipod increases with time in the first 120 min, and declines slightly from 120 to 180 min, likely due to the ripening of thin branches with high surface energy at elevated temperature (180 °C). We have tracked elemental transitions and size variations of Pt-Cu multipods during growth and found the nonlinear variations of the elemental content of Pt and Cu during growth. Based on the results, we can conclude that the element specific growth may be responsible for the morphology transformation and different growth rate, may also be the associated reason for the subsequent morphology evolution in other similar synthesis of Pt-Cu nanostructures, such as hollow nanocrystals, nanoframes and so on, during one-pot synthesis.[24, 37] The as-formed Pt-Cu alloy or even Cu-rich phase would be the precondition for galvanic replacement with Pt precursors to form the hollow structures.

The growth of Pt-Cu multipods in group II (30 : 1) was also quantitatively analyzed in Fig. 2B, showing the similar tendency as in group I. The concentration of Pt in early growth stage (e.g. 2 min, the atomic percent of Pt is ~68%) is slightly higher than that in the group I (9 : 1) (the atomic percent of Pt at 2 min is ~63%). The concentration of Pt declines from ~69% to ~55% during the first 65 min. After 65 min, the concentration of Pt starts to increase gradually from ~55% to ~97% till the end of the growth (180 min). The turning point here at 65 min is slightly later than that at 60 min in group I.

From the atomic quantification of Pt-Cu multipods by EDS analysis in group I and group II, we can divide the growth trajectories into three stages. In the first 20 min, the Pt-Cu nanocrystals with the content of Pt as high as >60% have generated (stage 1, marked as green background in Fig. 2). In the 20-30 min, the content of Pt decreased from 60 to 50%, and its content of ~50% lasts for about 30 min (stage 2, marked as blue background in Fig. 2). After 60 min, the content of Pt increases to 90% (stage 3, marked as yellow background in Fig. 2). The most likely causes for this evolution are given here. In stage 1, the Pt content is higher than that in stage 2. If we use $Pt(acac)_2$ or $Cu(acac)_2$ as precursors separately while keeping the other experimental conditions the same as the standard procedure, $Pt(acac)_2$ can be reduced to form Pt nanocrystals without a Cu precursor, whereas $Cu(acac)_2$ is very difficult to be reduced into Cu in the absence of $Pt(acac)_2$ (Fig. S6). Combined this result and the knowledge of Cu UPD on Pt, we deduce that Pt^{2+} ions is firstly reduced by OAm due to its relatively positive standard redox potential (e.g., 1.188 V for Pt^{2+}/Pt and 0.340 V for Cu^{2+}/Cu versus Reversible Hydrogen Electrode), and then the as-formed Pt induces the reduction of Cu^{2+} ions by taking advantage of Cu UPD, resulting in the formation of Pt-Cu alloy by co-reduction of the Pt and Cu precursors.[31, 40-42] The decrease of Pt content in stage 2 indicates that the reduction rate of Pt^{2+} ions is

slower than that of Cu^{2+} ions, which can be attributed to two possible reasons. One is that the addition of Br^- ions and amine group has a stronger complexing with Pt^{2+} ions than Cu^{2+} ions, resulting in the slower reduction rate of Pt^{2+} ions relative to Cu^{2+} ions.[40] Similar results have been obtained by other groups in synthesis of Pt-Cu nanocrystals in OAm.[24, 38, 43] The other reason is that the introduction of Br^- ions can dramatically promote the UPD of Cu on Pt, leading to the accelerated reduction rate of Cu^{2+} ions.[32] Both of them might be responsible for the decrease of Pt content in stage 2. In stage 3, most of Cu precursor was depleted and Pt rich branches grew up to form multipods.

As for the size variation here, the average size in the final product of group II (30 : 1) is much smaller than group I (9 : 1) (1100 nm^2 vs. 3750 nm^2, depicted as black rhombuses in Fig. 2B and 2A, separately). The average size evolution of group III is also depicted in Fig. 2A (the half-hollow dots and the dotted lines). STEM images of Pt dendrites in group III are shown in Fig. S7. Comparing the three groups, the average size and growth rate of multipods in group I (9 : 1) are higher than group II (30 : 1) and III (no Cu). The size variation in three groups can be attributed to the different reaction rates related with the amount of the Cu precursor. Since the formation of PtCu alloy can decrease the Gibbs free energy of this system, the introduction of small amount of Cu precursor can dramatically accelerate the reaction rate, leading to the highest size in group I. In addition to the difference in particle size, the branches with higher aspect ratio extended out from the core in group I are more regular and straight than those in group II and III. The straight branches (i.e., pods) are epitaxially formed through preferential overgrowth assisted by UPD of Cu on the specific surface of Pt.

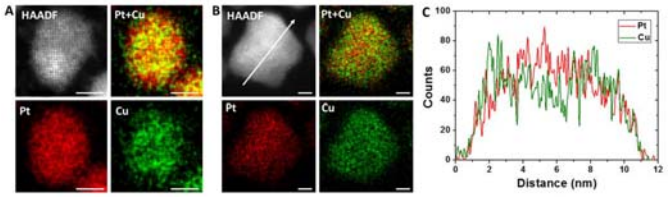

Fig. 3 HAADF-STEM and EDS characterizations Pt-Cu multipods of group I (9 : 1) at (A) 2 min and (B) 10 min. The monotonic figures in A and B are HAADF-STEM images, and the rest pictures are elemental distributions of Pt and Cu. The scale bars are 2 nm. (C) Line scan of Pt and Cu elements at the marked position of the HAADF-STEM image in B.

To further clarify the detailed distribution of Pt and Cu, STEM and EDS mapping images at higher magnification of Pt-Cu nanostructures in group I (9 : 1) at the initial growth period were obtained, as shown in Fig. 3. At 2 min (Fig. 3A), the small particle exhibits the flat and round surface with single crystal structure. From the EDS mapping images in Fig. 3A, the distribution of Pt is relatively uniform, while, Cu element distributes randomly around the nanocrystals. When the nanocrystals grow continually, they start to form protuberant parts around nanocrystals (Fig. 3B). In Fig. 2A, the statistic analysis shows that the concentration of Pt decreases along the growth process from the beginning of the primarily nucleated small particles to around 60 min. In Fig. 3B and 3C, it can be seen that the distribution of Pt is slightly higher in the middle part. Correspondingly, the distribution of Cu is sparse in the middle part than in the outside. The Pt-rich core is 2~3 nm in size and approximately $Pt_{65}Cu_{35}$ in composition, similar with nucleated nanocrystals at 2 min. Similar result has also been observed in group II (Fig. S8).

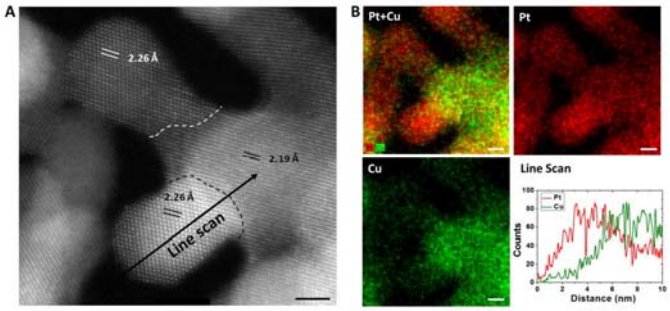

Fig. 4 HAADF-STEM and EDS characterizations of Pt-Cu multipods of group I (9 : 1) at 70 min. (A) High resolution STEM image of branched area of a Pt-Cu multipod. (B) EDS mapping and the elemental distribution of Pt (red) and Cu (green) and the line profiles taken along the direction marked with a black arrow in A. All the scale bars are 2 nm.

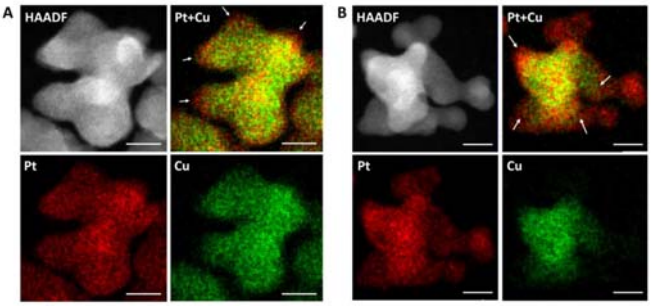

Fig. 5 HAADF-STEM and EDS characterizations of Pt-Cu multipods of group II (30 : 1) at (A) 65 and (B) 100 min. All the scale bars are 5 nm. The grown Pt-rich layer is thicker in bulging area as pointed with white arrows.

After 60 or 65 min, the atomic percent of Pt abruptly increases, indicating the different growth behavior of Pt and Cu. This variation could be attributed to the corresponding dynamical transformation of growth conditions. To gain atomic- and element-specific details into the growth morphologies of Pt-Cu multipods, the detailed characterizations of Pt-Cu multipod (both 9 : 1 and 30 : 1) during the regrowth of Pt-rich phase were carried out in Fig. 4 and Fig. 5. Fig. 4A is an enlarged STEM image of a typical Pt-Cu multipod (9 : 1) at 70 min accompanied with EDS mapping of Pt and Cu on the right side. The configuration of the whole Pt-Cu multipod was shown in Fig. S9. From the EDS mapping images, it can be seen that the two branches are mainly composed of Pt element due to the depletion of Cu precursor in the formation of Pt-Cu alloy. From the HAADF-STEM images, Pt rich branches were epitaxially grew on Pt-Cu alloy. For a system involving Pt and Cu, the interplaner spacing of Pt (111) and Cu (111) are 2.27 and 2.09 Å, respectively, so the theoretical lattice mismatch of Pt-rich phase (e.g. 85% Pt and 15% Cu, 2.24 Å from EDX quantification of Pt-rich branch area) and Pt-Cu alloy (e.g. 50% Pt and 50% Cu, 2.18 Å from EDX quantification of Pt-Cu alloy main body area) is 2.8% according

to Vegnard's Law. The experimental lattice mismatch of Pt-rich phase from the branch area (2.26 Å) and Pt-Cu alloy from the main body area (2.19 Å) is 3.2%, which is close to the calculated value. As a result, the small lattice mismatch between the branches and mainbody lead to the development of Pt-Cu multipods with Pt-rich branches epitaxially grew on the Pt-Cu alloy cores.

Correspondingly, morphological and elemental specifics of Pt-Cu multipods in group II (30 : 1) obtained at 65 and 100 min have been characterized in Fig. 5. At 65 min in Fig. 5A, the distribution of Pt is slightly larger than that of Cu. It can be deduced that Pt-rich phase grow simultaneously around the Pt-Cu alloy nanostructures. With further analysis, we can see that the grown Pt-rich layer is thicker in bulging area as pointed with white arrows marked in Fig. 5A than other flat and concave areas. After growing for a certain amount of time (e.g. 100 min in Fig. 5B), the Pt-rich bulging islands may keep growing, and even evolve into the branches (illustrated with white arrows in Fig. 5B), while the remaining flat and concave areas with a thin Pt-rich layers would nearly stop growing.

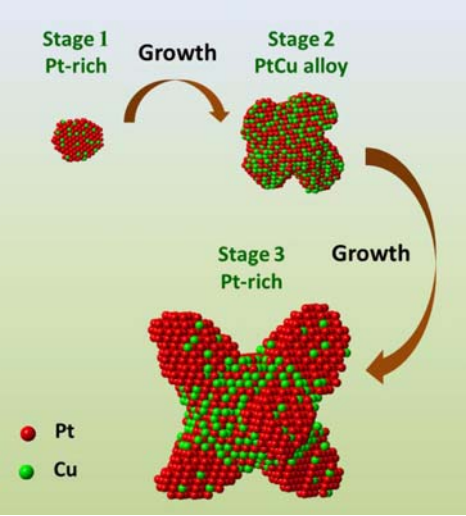

Fig. 6 Schematic illustration of the growth trajectories of Pt-Cu multipods in different stages summarized from HAADF-STEM and EDS characterizations.

A comprehensive growth behavior model of Pt-Cu bimetallic multipods in different stages is summarized in Fig. 6. At the first 20 min, the Pt-rich seeds exist because Pt^{2+} ions are firstly reduced due to its relatively positive standard redox potential relative to Cu^{2+} ions. After that, Pt-Cu alloy petals grow on Pt-rich seeds because of the UPD effect of Cu atoms on Pt substrates and the complex effect of Pt^{2+} ions with Br^- ions from CTAB and amine group from OAm. After depletion of Cu precursors at about 60~65 min, Pt-rich branches start to epitaxially grow on Pt-Cu alloy cores. At this time, galvanic replacement between Pt^{2+} ions with Cu atoms in Pt-Cu alloy cores may happen. Finally, the Pt-Cu multipods were generated through the continuing growth of Pt-rich branches.

4. Conclusion

For bimetallic nanocrystals with an alloy structure, the elemental distribution of two metals throughout the nanocrystals, especially on the surface, plays an important role in determining the catalytic properties for a rich variety of the reactions. Owing to the different redox potential of two metals in combination with the interaction between them (e.g., UPD, galvanic replacement, and phase segregation), however, it is difficult to generate an alloy nanocrystal with homogeneous element distribution as expected. In addition, the composition variation generally accompanies the morphology evolution, which is also a key parameter for a given catalytic reaction. The present study on the growth trajectories of Pt-Cu multipods at different stages through aberration-corrected HAADF-STEM with EDS mapping provides a comprehensive understanding towards their composition and morphology evolutions as well as the related mechanism during the synthesis. This work provides a versatile and powerful method to reveal the growth dynamics of bimetallic nanocrystals, which can bring into full play in other multi-element systems.

Acknowledgements

We acknowledge Prof. Yawen Zhang from Peking University for fruitful suggestions, and the access to microscope facilities provided by the Center of Electron Microscopy of Zhejiang University. This work is financially supported by the National Science Foundation of China (51222202, 51372222, 51472215, 61172011 and 61571197), the National Basic Research Program of China (2014CB932500 and 2015CB921000), the Program for Innovative Research Team in University of Ministry of Education of China (IRT13037 and IRT13R54) and the Fundamental Research Funds for the Central Universities (2014FZA4007 and 2014XZZX003-07). Z. Y. L. thanks the Qiushi Foundation for a Chair Professorship in Zhejiang University.

Notes and references

1 D. Wang and Y. Li, *Adv. Mater.*, 2011, **23**, 1044.
2 S. E. Habas, H. Lee, V. Radmilovic, G. A. Somorjai and P. Yang, *Nat. Mater.*, 2007, **6**, 692.
3 F.-R. Fan, D.-Y. Liu, Y.-F. Wu, S. Duan, Z.-X. Xie, Z.-Y. Jiang and Z.-Q. Tian, *J. Am. Chem. Soc.*, 2008, **130**, 6949.
4 J. A. Rodriguez and D. W. Goodman, *Science*, 1992, **257**, 897.
5 M. Jaime, R. Movshovich, G. R. Stewart, W. P. Beyermann, M. G. Berisso, M. F. Hundley, P. C. Canfield and J. L. Sarrao, *Nature*, 2000, **405**, 160.
6 K. Gschneidner, A. Russell, A. Pecharsky, J. Morris, Z. H. Zhang, T. Lograsso, D. Hsu, C. H. C. Lo, Y. Y. Ye, A. Slager and D. Kesse, *Nature Mater.*, 2003, **2**, 587.
7 T. Krenke, E. Duman, M. Acet, E. F. Wassermann, X. Moya, L. Manosa and A. Planes, *Nature Mater.*, 2005, **4**, 450.
8 S. E. Habas, H. Lee, V. Radmilovic, G. A. Somorjai and P. Yang, *Nature Mater.*, 2007, **6**, 692.
9 D. Xu, Z. P. Liu, H. Z. Yang, Q. S. Liu, J. Zhang, J. Y. Fang, S. Z. Zou and K. Sun, *Angew. Chem. Int. Ed.*, 2009, **48**, 4217.
10 B. D. Adams, G. Wu, S. Nigro and A. Chen, *J. Am. Chem. Soc.*, 2009, **131**, 6930.
11 K. Zhou and Y. Li, *Angew. Chem. Int. Ed.*, 2012, **51**, 602.
12 H. Zhang, M. Jin and Y. Xia, *Chem. Soc. Rev.*, 2012, **41**, 8035.

13 N. S. Porter, H. Wu, Z. Quan and J. Fang, *Acc. Chem. Res.*, 2013, **46**, 1867.
14 S. Sun, C. B. Murray, D. Weller, L. Folks and A. Moser, *Science*, 2000, **287**, 1989.
15 Z. R. Dai, S. Sun and Z. L. Wang, *Nano Lett.*, 2001, **1**, 443.
16 J. Zhang and J. Fang, *J. Am. Chem. Soc.*, 2009, **131**, 18543.
17 K. E. Elkins, T. S. Vedantam, J. P. Liu, H. Zeng, S. Sun, Y. Ding and Z. L. Wang, *Nano lett.*, 2003, **3**, 1647.
18 E. V. Shevchenko, D. V. Talapin, H. Schnablegger, A. Kornowski, Ö. Festion, P. Svedlindh, M. Haase and W. Horst, *J. Am. Chem. Soc.*, 2003, **125**, 9090.
19 D. C. Lee, F. V. Mikulec, J. M. Pelaez, B. Koo and B. A. Korgel, *J. Phys. Chem. B*, 2006, **110**, 11160.
20 J. R. C. Salgado, E. Antolini and E. R. Gonzalez, *J. Phys. Chem. B*, 2004, **108**, 17767.
21 E. V. Shevchenko, D. V. Talapin, A. L. Rogach, A. Kornowski and M. Haase. *J. Am. Chem. Soc.*, 2002, **124**, 11480.
22 C. Cui, L. Gan, H.-H. Li, S.-H. Yu, M. Heggen and P. Strasser, *Nano lett.*, 2012, **12**, 5885.
23 Y. Chen, F. Yang, Y. Dai, W. Wang and S. Chen, *J. Phys. Chem. C*, 2008, **112**, 1645.
24 B. Y. Xia, H. B. Wu, X. Wang and X. W. Lou, *J. Am. Chem. Soc.*, 2012, **134**, 13934.
25 Y. Kang and C. B. Murray, *J. Am. Chem. Soc.*, 2010, **132**, 7568.
26 V. Radmilovic, H. A. Gasteiger and P. N. Ross. *J. Catal.*, 1995, **154**, 98.
27 M. Schrinner, M. Ballauff, Y. Talmon, Y. Kauffmann, J. Thun, M. Möller and J. Breu, *Science*, 2009, **323**, 617.
28 B. Lim, M. Jiang, P. H. C. Camargo, E. C. Cho, J. Tao, X. Lu, Y. Zhu and Y. Xia, *Science*, 2009, **324**, 1302.
29 A.-X. Yin, X.-Q. Min, Y.-W. Zhang and C.-H. Yan, *J. Am. Chem. Soc.*, 2011, **133**, 3816.
30 J. Fennell, D. He, A. M. Tanyi, A. J. Logsdail, R. L. Johnston, Z. Y. Li and S. L. Horswell, *J. Am. Chem. Soc.*, 2013, **135**, 6554.
31 Y. Jiang, Y. Jia, J. Zhang, L. Zhang, H. Huang, Z. Xie and L. Zheng, *Chem. Eur. J.*, 2013, **19**, 3119.
32 A.-X. Yin, X.-Q. Min, W. Zhu, W.-C. Liu, Y.-W. Zhang and C.-H. Yan, *Chem. Eur. J.*, 2012, **18**, 777.
33 Y. Qi, T. Bian, S.-I. Choi, Y. Jiang, C. Jin, M. Fu, H. Zhang and D. Yang. *Chem. Commun.*, 2014, **50**, 560.
34 X. Liu, W. Wang, H. Li, L. Li, G. Zhou, R. Yu, D. Wang and Y. Li, *Sci. Rep.*, 2013, **3**.
35 Y. Jia, Y. Jiang, J. Zhang, L. Zhang, Q. Chen, Z. Xie and L. Zheng, *J. Am. Chem. Soc.*, 2014, **136**, 3748.
36 F. Saleem, Z. Zhang, B. Xu, X. Xu, P. He and X. Wang, *J. Am. Chem. Soc.*, 2013, **135**, 18304.
37 F. Nosheen, Z. Zhang, J. Zhuang and X. Wang, *Nanoscale*, 2013, **5**, 3660.
38 X. Yu, D. Wang, Q. Peng and Y. Li, *Chem. Commun.*, 2011, **47**, 8094.
39 Y. Kuang, Z. Cai, Y. Zhang, D. He, X. Yan, Y. Bi, Y. Li, Z. Li and X. Sun, *ACS Appl. Mater. Interfaces*, 2014, **6**, 17748.
40 J. G. Speight, *Lange's Handbook of Chemistry, 16th ed.*, McGraw-Hill, New York, USA 2005.
41 G. Jerkiewicz, F. Perreault and Z. Radovic-Hrapovic, *J. Phys. Chem. C*, 2009, **113**, 12309.
42 Z.-L. Wu and S. L. Yau, Langmuir, 2001, **17**, 4627.
43 S.-B. Wang, W. Zhu, J. Ke, J. Gu, A.-X. Yin, Y.-W. Zhang and C.-H. Yan, *Chem. Commun.*, 2013, **49**, 7168.

Table of Contents

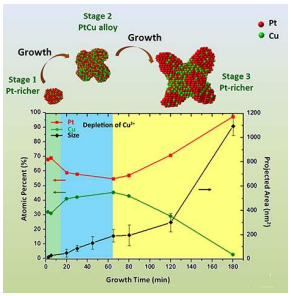

An element-specific growth trajectories of PtCu multipods nanostructures with compositional and morphological variation was revealed by HAADF-STEM and EDS mapping.